



Heriot-Watt University
Research Gateway

Network sensor calibration for retrieving accurate moment tensors of acoustic emissions

Citation for published version:

Davi, R, Vavrycuk, V, Charalampidou, EM & Kwiatek, G 2013, 'Network sensor calibration for retrieving accurate moment tensors of acoustic emissions', *International Journal of Rock Mechanics and Mining Sciences*, vol. 62, pp. 59-67. <https://doi.org/10.1016/j.ijrmms.2013.04.004>

Digital Object Identifier (DOI):

[10.1016/j.ijrmms.2013.04.004](https://doi.org/10.1016/j.ijrmms.2013.04.004)

Link:

[Link to publication record in Heriot-Watt Research Portal](#)

Document Version:

Peer reviewed version

Published In:

International Journal of Rock Mechanics and Mining Sciences

General rights

Copyright for the publications made accessible via Heriot-Watt Research Portal is retained by the author(s) and / or other copyright owners and it is a condition of accessing these publications that users recognise and abide by the legal requirements associated with these rights.

Take down policy

Heriot-Watt University has made every reasonable effort to ensure that the content in Heriot-Watt Research Portal complies with UK legislation. If you believe that the public display of this file breaches copyright please contact open.access@hw.ac.uk providing details, and we will remove access to the work immediately and investigate your claim.

Network sensor calibration for retrieving accurate moment tensors of acoustic emissions

Rosalia Davi¹, Václav Vavryčuk¹, Elli-Maria Charalampidou², Grzegorz Kwiatek²

¹*Institute of Geophysics, Academy of Sciences, Boční II/1401, 14100 Praha 4, Czech Republic*

²*Helmholtz Centre Potsdam, GFZ German Research Centre for Geosciences, Telegrafenberg, D14473 Potsdam, Germany*

Abstract

In this paper, we apply a method for retrieving accurate moment tensors in the acoustic emission (AE) experiments based on the joint inversion of a family of AE events for their moment tensors and for the sensor amplifications including coupling effects between sensors and a specimen. The accuracy and efficiency of the method is tested on AEs recorded during three different temporal stages of a triaxial compression experiment on a cylindrical Bentheim sandstone specimen. The results show improved quality of the moment tensors indicated by significantly lower root-mean-square residuals between observed and predicted amplitudes. The approach is particularly suitable for detailed studies of the source parameters of AE events, to obtain accurate focal mechanisms and seismic moment tensors and for detecting fracturing regime of microcracks.

Keywords: acoustic emissions, focal mechanisms, fracturing, moment tensors, sensor calibration

1. Introduction

Moment tensor inversion is one of the basic tools for analyzing source mechanisms of tectonic and volcanic earthquakes observed in the Earth's crust, but also of acoustic emissions (AEs) recorded in laboratory environments [1-8]. Although AEs and earthquakes are different in size, strength and radiated frequencies, the physics of the source and the source mechanisms are basically similar and the moment tensors can provide insights into fracture processes on all these scales. The double-couple (DC) and non-double-couple (non-DC) components of the moment tensors are, in particular, important when studying: (1) the orientation and geometry of micro-cracks, cracks, fractures or faults, (2) physical properties of rocks in the focal zone, and (3) the shear/tensile type of fracturing [9-11]. In addition, the moment tensors provide valuable information on the stress field in the focal zone.

Similarly as for earthquakes, moment tensor inversion of AEs is a data-demanding procedure which requires an accurate velocity model, accurate locations and high-quality data with a high signal-to-noise ratio, recorded by many sensors with good azimuthal coverage. In earthquake seismology, the difficulties in the moment tensor inversion usually arise because of unfavorable station configurations and inaccurate and simplistic velocity models used,

which can produce numerical errors in the inversion. In contrast to observations of earthquakes, the velocity model can be measured quite accurately in AE experiments and also the configuration of sensors can be designed to be optimum. However, we often meet with a problem of poorly known amplitudes of recordings when inverting AEs because the sensor calibration is often inaccurate and/or the coupling effects between the sensors and the specimen are usually neglected. Since measuring correct amplitudes is a key factor in determining accurate moment tensors, this problem must be addressed and solved in all advanced studies of acoustic emissions.

Recently, a new method which solves the problem of the sensor calibration was proposed by Davi and Vavryčuk [12] and tested on seismic data. The method is called the network calibration and it is based on a joint inversion of a family of seismic events for their moment tensors and for sensor amplifications. The method proved to be an efficient way to determine or to correct the sensor amplifications in order to retrieve highly accurate moment tensors of earthquakes. In this paper, the method is applied to AE data at laboratory scale. The results show an improved quality of the retrieved moment tensors indicated by significantly lower root-mean-square (RMS) residuals between observed and predicted amplitudes if the network calibration is performed. The improvement of accuracy is particularly visible when analysing the non-DC components of the moment tensors, which are important for interpretations and understanding of source processes [9,11,13-16].

2. Method

The standard moment tensor inversion of amplitudes for one individual event is based on the following equation:

$$\mathbf{G}\mathbf{m} = \mathbf{u}, \quad (1)$$

where \mathbf{G} is the $N \times 6$ matrix of the spatial derivatives of the Green's function amplitudes,

$$\mathbf{G} = \begin{bmatrix} \mathbf{g}^{(1)} \\ \mathbf{g}^{(2)} \\ \dots \\ \mathbf{g}^{(N)} \end{bmatrix} = \begin{bmatrix} G_1^{(1)} & G_2^{(1)} & G_3^{(1)} & G_4^{(1)} & G_5^{(1)} & G_6^{(1)} \\ G_1^{(2)} & G_2^{(2)} & G_3^{(2)} & G_4^{(2)} & G_5^{(2)} & G_6^{(2)} \\ \dots & \dots & \dots & \dots & \dots & \dots \\ G_1^{(N)} & G_2^{(N)} & G_3^{(N)} & G_4^{(N)} & G_5^{(N)} & G_6^{(N)} \end{bmatrix}, \quad (2)$$

\mathbf{m} is the vector composed of 6 components of moment tensor \mathbf{M} ,

$$\mathbf{m} = [M_{11} \quad M_{22} \quad M_{33} \quad M_{23} \quad M_{13} \quad M_{12}]^T, \quad (3)$$

and \mathbf{u} is the vector of displacement amplitudes observed at N one-component sensors. Quantities $G_k^{(i)}$ are the components of the Green's function matrix for the i th sensor:

$$\begin{aligned} G_1 &= G_{1,1}, \quad G_2 = G_{2,2}, \quad G_3 = G_{3,3}, \\ G_4 &= G_{2,3} + G_{3,2}, \quad G_5 = G_{1,3} + G_{3,1}, \quad G_6 = G_{1,2} + G_{2,1}, \end{aligned} \quad (4)$$

where $G_{k,m}$ means the spatial derivative of the Green's function produced by the force along the k -axis and oriented along the sensor direction. The superscript i identifying the sensor is omitted.

If we incorporate one sensor of an unknown amplification with index $i = N+1$ into the inversion, we can put:

$$\mathbf{g}^{(N+1)} \mathbf{m} = C^{(N+1)} u^{(N+1)}, \quad (6)$$

where $C^{(N+1)}$ is the unknown amplification, and $\mathbf{g}^{(N+1)}$ is defined as follows:

$$\mathbf{g}^{(N+1)} = \begin{bmatrix} G_1^{(N+1)} & G_2^{(N+1)} & G_3^{(N+1)} & G_4^{(N+1)} & G_5^{(N+1)} & G_6^{(N+1)} \end{bmatrix}. \quad (7)$$

Combining equations (1) and (6) we obtain the following equation for moment vector \mathbf{m} and amplification $C^{(N+1)}$:

$$\begin{bmatrix} \mathbf{G} & \mathbf{0} \\ \mathbf{g}^{(N+1)} & -u^{(N+1)} \end{bmatrix} \cdot \begin{bmatrix} \mathbf{m} \\ C^{(N+1)} \end{bmatrix} = \begin{bmatrix} \mathbf{u} \\ 0 \end{bmatrix}. \quad (8)$$

Obviously, a similar system of equations can be written for the inversion for moment tensors of many events and for the amplifications of many sensors [12]. For illustration, if 10 events recorded at 10 sensors with known amplification are inverted for moment tensors, the joint inversion is based on solving a system of 100 equations for 60 unknowns that is a well overdetermined problem. If 10 events recorded at 1 sensor with known amplification and at 9 sensors of unknown amplification are inverted for moment tensors and amplifications, a system of 100 equations is solved for 69 unknowns that is still an overdetermined problem. In principle, it is permissible that all sensors are of unknown amplification and we can still invert for moment tensors and for the sensor amplifications. In this case, however, the inversion yields the relative moment tensors and the relative sensor amplifications only. The scalar moments and the absolute sensor amplifications cannot be determined.

As for the standard moment tensor inversion, the joint inversion works properly if the following conditions are satisfied: (1) the network of sensors must ensure a dense coverage of the focal sphere, (2) amplitudes of events must have a good signal-to-noise ratio, (3) the propagation velocity within the specimen must be known with the highest accuracy as possible, and (4) event locations must be accurate. In addition, extensive datasets of events, displaying a variety of focal mechanisms, are required so as the system of equations to be well overdetermined. In order to increase the accuracy of the amplifications, the inversion can be performed in iterations (for details, see [12]). In this case, the sensor amplifications are calculated repeatedly with gradually increasing accuracy. If the difference between the amplifications from the previous and the current iterations are less than a prescribed error, the iteration process is stopped. If no sensor amplification is known before the calibration, the average of the sensor amplifications must be fixed in the inversion.

3. Experiment setup and AE hypocentre locations

The method is exemplified on acoustic emissions recorded during a triaxial compression experiment carried out at the GFZ Potsdam. The experiment was performed on a cylindrical Bentheim sandstone specimen (50 mm diameter and 105 mm in length) with a notch in its mid-height. The specimen was initially loaded under isotropic compression (up to 160 MPa confining pressure) and subsequently under deviatoric compression (with a displacement control at a rate of 20 $\mu\text{m}/\text{min}$) up to almost 1.2% of axial strain, before being fully unloaded. Compaction bands were formed in this specimen, alike what has been also observed in other porous sandstones being subjected to similar stress states [17,18]. A detailed description of the experimental results as well as the formation and evolution of the developed compaction bands is not the subject of this paper and it will be published in another paper.

Sixteen P-wave sensors were glued to the surface of the specimen, providing a good azimuthal coverage, and two P-wave sensors (embedded in two metallic spacers) were placed at its top and bottom boundaries. These AE sensors were made of piezoceramic disks of 2 mm thickness and 5 mm diameter and had a resonant frequency of 1 MHz. Fig. 1 illustrates the positions of these sensors on the surface of the Bentheim specimen. During the experiment, all AE sensors were connected to a 16 channel transient acquisition system (DAXBox, PRÖKEL, Germany), which worked in a continuous mode recording either AE or ultrasonic transmissions (for more details see [17,19]). During the latter measurement, half of the sensors (shown in red in Fig. 1b) were emitting consecutively every 30 s a rectangular pulse of 100 V in amplitude and 3 μs in duration. These pulses were recorded on the remaining sensors (ultrasonic receivers, shown in blue in Fig. 1b), forming 65 individual ultrasonic transmitter-receiver traces across the specimen during each ultrasonic transmission measurement (pulses of 8 transmitters recorded at 8 receivers plus one trace of the sensor pair 16-15, because pulses of transmitter 16 were recorded only by receiver 15).

The recorded waveforms were processed in the following way. Both AE and ultrasonic transmission waveforms were automatically discriminated. The P-wave onset times were measured by applying an automatic picking algorithm, based on the Akaike information criterion [20], and the first P-wave amplitudes were automatically captured for both AE and ultrasonic transmission waves. Time-dependent 1D-velocity layered model was estimated based on ultrasonic transmission data. The AE hypocentre locations were calculated by minimizing the travel time residuals, using the downhill simplex algorithm [21] and taking into account the velocity model estimated from the ultrasonic velocity measurements.

Fig. 2 shows the ultrasonic transmission velocities measured along rays between 6 transmitter-receiver pairs as a function of time during the experiment. Sensors 15-16 measured velocities along the length of the specimen. Ultrasonic velocities decrease in time, which indicates the creation of damage in the specimen. The velocity reduction is, however, rather small being less than 2%. In addition, the damage in the specimen produces seismic

anisotropy, which gradually increases with time. But its strength is also small being less than 1% even at later stages of the experiment.

Three different time stages have been selected to illustrate the efficiency of the presented network calibration method. The hypocentre locations of AE events recorded during these three stages and during the whole deviatoric loading stage are shown in Fig. 3. In all cases, a concentration of hypocentre locations is observed in the mid-height of the specimen due to the existence of the notch, which facilitated the formation and propagation of compaction bands [see also 17,18]. The location accuracy of the AE events was estimated from travel-time residuals being about 2 mm.

4. Sensor calibration

4.1. Calibration using ultrasonic transmission data

The amplitudes of the ultrasonic transmission (UT) first P-wave pulses were used to assess the coupling quality of the sensors. The applied calibration procedure (called as ‘ultrasonic calibration’) estimates the coupling correction factors of all sensors and provides information on incidence angle correction.

The amplitude A_{ij} of an ultrasonic pulse emitted by the ultrasonic transmitter i and recorded at the ultrasonic receiver j is modelled according to the following equation:

$$A_{ij} = \frac{1}{r} \exp(-a\alpha^{2b}) S_i S_j, \quad (9)$$

where r is the distance between the ultrasonic transmitter-receiver pair (correction for the geometrical spreading assuming the isotropic environment), S_i and S_j are the amplification factors (coupling factors) for ultrasonic transmitter and receiver, respectively. The exponential term is responsible for the incidence angle correction of the ultrasonic receiver and for the take-off-angle correction of the ultrasonic transmitter. As the straight ray paths between transmitter and receiver are assumed, both angles are equal resulting in the exponential term in equation (9) being squared. The α coefficient is the angle of incidence to the ultrasonic transmitter (or accordingly, the take-off angle of the ultrasonic transmitter) and a and b are the coefficients defining variations of recorded amplitudes with incidence/take-off angles. We invert for coupling coefficients S_i and S_j as well as for a and b parameters by comparing the observed ultrasonic transmission amplitudes between different ultrasonic transmitters and receivers with those predicted by equation (9).

The calibration procedure was performed for Bentheim sandstone using the ultrasonic transmission measurements of 14 sensors (sensors 15, 16, 17 and 18 were excluded) recorded in the first part of the experiment (time < 4000 s). Fig. 4a presents the uncalibrated (raw) amplitudes of pulses emitted by 7 transmitters and recorded at 7 receivers as a function of incidence angle, whereas Fig. 4b displays the amplitudes already calibrated for the coupling effects together with the estimated common calibration curve. The comparison of Figs 4a and

4b provides clear evidence that three sensors display major coupling problems (sensors 8, 10, 13) with estimated amplification factors standing 3.24, 3.37 and 2.43. It is therefore expected that the quality of moment tensor solutions is lower while raw amplitudes are used.

In the following section, we considered two versions of the same dataset: a) with raw amplitudes corrected only for the incidence angle, and b) with amplitudes corrected for the incidence angle and for the UT-calibration amplitude corrections.

4.2. Calibration using the joint inversion for amplifications and moment tensors

The calibration using the joint inversion ('network calibration') has been applied to three selected temporal stages of the recorded data (see Fig. 3b-3d). The amplitudes of P-waves of the AE events recorded by the full set of 14 sensors were inverted. The Green's function amplitudes were calculated using ray method [22] and incorporated the effects of the free surface. The velocity model was homogeneous and isotropic and the rays were straight lines. Using the homogenous velocity model is justified as the highly damaged zone is limited to the relatively thin area bounding the compaction band. Hence, the rays passed mainly the remaining part of the sample where the velocities are decreasing only slowly and uniformly throughout the experiment. Moreover, differences in the P-wave velocities for different ray paths are very small, so the velocity anisotropy of the sample can also be neglected (see Fig. 2). The stages counted 1250, 5500 and 3750 events. The three datasets were further divided into subsets of 250 events; hence the total number of subsets was 42. We adopted the value of 250 events for each subset as a trade-off between computational cost and the need of ensuring high variability of focal mechanisms in order to determine the sensor amplifications with a sufficiently high accuracy. The number of iterations of the inversion process was fixed to 25. The sensor amplifications were calculated for all 42 subsets using raw data ('amplifications of uncalibrated sensors') and data ultrasonically calibrated as described in Section 4.1 ('amplifications of calibrated sensors').

Figs 5 and 6 summarize the retrieved amplifications of individual sensors, for both raw and calibrated data. If the ultrasonic calibration (see Section 4.1.) is sufficiently accurate and equivalent to the network calibration, the network calibration using the raw data should yield identical amplifications as the ultrasonic calibration, and the network calibration using the ultrasonically calibrated data should yield amplifications equal to 1. However, Figs 5 and 6 indicate visible differences between both calibration procedures:

- (1) The amplification values of the network calibration retrieved for each sensor show a very similar trend in the selected time intervals. This proves a robustness of the network calibration and a high degree of time-stability of the amplifications.
- (2) The amplifications retrieved using the network calibration show roughly similar trends as those retrieved using the ultrasonic calibration. Both calibration procedures confirmed that AE sensors 8, 10 and 13 are badly coupled and require a significant correction, which is reflected in high values of recovered amplification factors (see Fig. 5).

(3) As expected, the amplification corrections produced by the network calibration are closer to 1 if the ultrasonically calibrated data are used (see Fig. 6), especially for the sensors with bad coupling.

Fig. 7 shows a detailed temporal variation of retrieved amplifications for three selected sensors (1, 11, and 13, see Fig. 1b). The amplifications of the selected uncalibrated sensors (in blue) display a scatter with values between 0.6 and 2. Nevertheless, these values are quite stable when calculated for different subsets of events. The amplifications of the selected ultrasonically calibrated sensors (in red) are less scattered ranging between 0.8 and 1.1 and also the variation of sensor amplifications for different subsets of events is less pronounced than for raw data (see Fig. 7). Since the retrieved amplifications are consistent for all 42 subsets and display no significant variation in time, we can conclude that:

- (1) The network inversion was successful and yields reliable amplification values for all sensors.
- (2) The coupling effects between the sensors and specimen are similar in all three stages of the experiment. Hence, we do not observe any significant evolution of the coupling effects in time.
- (3) The ultrasonic calibration of sensors improved the quality of the data, because the amplifications of calibrated sensors are closer to 1 when compared with amplifications of uncalibrated sensors.
- (4) Even if the quality of the ultrasonically calibrated data is much higher than that of the raw data, the accuracy of the sensor amplifications can be still further improved by applying the network calibration.

The accuracy of the final sensor amplifications can be estimated using the jack knife approach described by Davi and Vavryčuk [12]. For each stage, we run the iterative procedure 50 times for 100 randomly chosen events and calculate the mean value and the standard deviation of the amplifications. The results obtained for Stage 1 are shown in Fig. 8. The standard deviations span from 0.02 to 0.05 for the majority of the calibrated sensors except for sensors 2 and 10 with the standard deviation about 0.07. The standard deviations of sensor amplifications calculated for raw data are about three times higher. This indicates that when the ultrasonic calibration is not available, it is still possible to determine the sensor amplifications but the highest accuracy is achieved when the inversion for amplifications is applied to ultrasonically calibrated data.

Since the sensor amplifications are characterized by a high stability in time, we decided to calculate the average values of amplifications over all subsets for each of the three stages. These values retrieved for uncalibrated (raw) and ultrasonically calibrated data are used to correct the amplitudes of the recorded waveforms and consequently to calculate accurate moment tensors of the AEs.

5. Moment tensors and their accuracy

In order to exemplify the effects of inaccurate amplitudes on the resultant moment tensors, we perform the moment tensor inversions of four different datasets of amplitudes. We invert the uncalibrated (raw) amplitudes, the amplitudes obtained using the ultrasonic calibration as described in Section 4.1., the corrected amplitudes using the network calibration of the raw data, and finally, the corrected amplitudes using the network calibration of the ultrasonically calibrated data. The moment tensors are decomposed into the double-couple (DC), isotropic (ISO) and compensated linear vector dipole (CLVD) components according to the formulas of Vavryčuk [16]. The quality of the results is evaluated through the analysis of the root-mean-square (RMS) residuals defined as the sum of the normalized differences between the synthetic and observed amplitudes at all sensors for the individual events. The dataset of the first stage is shown here as an example, stages 2 and 3 display similar trends.

Fig. 9 shows the DC and non-DC components of the uncorrected and corrected moment tensors for the uncalibrated data. A general pattern of the P and T axes (left-hand plots) is expected being produced by the deviatoric compression of the specimen during the experiment. The P axes have nearly vertical directions; the T axes are rather horizontal with no distinct azimuthal preference. The CLVD and ISO components are negative and indicate compressional mechanisms [11], which are associated with the presence of the compaction band in the specimen. Although the overall pattern of the DC and non-DC components is similar for corrected and uncorrected moment tensors, they differ in details. The corrected moment tensors show significantly lower values of RMS: the average RMS decreased from 0.3 for uncorrected moment tensors to 0.12 for corrected moment tensors. In addition, the non-DC components are more clustered for corrected moment tensors.

Similar trends are visible in Fig. 10 which shows the DC and non-DC components of uncorrected and corrected moment tensors for the ultrasonically calibrated data. Again, the corrected moment tensors display more clustered non-DC components and a lower value of the RMS. The average RMS is 0.17 for calibrated amplitudes and decreases after correction to a value less than 0.1. A detailed comparison of the RMS values for calibrated/uncalibrated data before and after corrections is shown in Fig. 11. The figure indicates a significant reduction of the RMS values after applying the ultrasonic calibration of amplitudes (Fig. 11b). However, the RMS is further reduced after applying the network calibration, which indicates that the accuracy of the resultant moment tensors is increased after corrections. The figure also indicates that avoiding the ultrasonic calibration procedure, which might sometimes be intricate and laborious, is possible. If the ultrasonic calibration is missing we can apply the network calibration to uncalibrated data and improve the accuracy of moment tensors. The accuracy is similar or even better than that obtained from ultrasonic calibration.

Discussion and conclusions

Accurate and undistorted recordings of AEs in laboratory experiments are a necessary condition for any advanced source studies and interpretations of moment tensors. A careful calibration of sensors including both their frequency response and a measurement of the coupling effects between the sensor and the specimen is required for such studies. This procedure is always a challenging task and a frequent source of inaccuracies. As shown in this paper, the presented method can solve the problem in an efficient and elegant way. By applying a joint inversion for sensor amplifications and moment tensors to a set of sufficiently large number of AEs (hundreds of events), we can determine the actual sensor amplifications including the coupling effects.

The calibration method applied to AEs recorded in a compaction band experiment performed on the Bentheim sandstone proved to produce accurate sensor amplifications. The increase of accuracy is indicated by lower RMS values between the synthetic and observed amplitudes in the moment tensor inversion. In addition, the non-DC components, which are in general very sensitive to numerical errors in the inversion, display visibly more compact clustering after applying the proposed calibration. If the ultrasonic calibration of sensors is available, the proposed joint inversion can be applied to calibrated data and further to improve their accuracy. In case of experiments performed under complicated or extreme stress regimes, when the coupling between the sensors and the specimen might change in time, the proposed method can retrieve time dependent sensor amplifications.

Acknowledgements

We thank one anonymous reviewer for his detailed and helpful comments. The experimental work was carried out by S. Stanchits and E-M. Charalampidou at the GFZ Potsdam as a part of the research project related to compaction band initiation and propagation in porous sandstones. We would like to thank S. Stanchits for his important involvement in the experiment and for his valuable comments on the paper, and S. Gehrman for the preparation of the Bentheim specimen. The work on the network calibration was supported by the Grant Agency of the Czech Republic, Grant P210/12/1491, and by the European Community's FP7 Consortium Project AIM "Advanced Industrial Microseismic Monitoring", Grant Agreement 230669.

References

- [1] Ohtsu M. Simplified moment tensor analysis and unified decomposition of acoustic emission sources: application to in situ hydrofracturing test. *J. Geophys. Res.* 1991; 96, B4: 6211–21.
- [2] Manthei G, Eisenblätter J, Dahm T. Moment tensor evaluation of acoustic emission sources in salt rock. *Constr. Build. Mater.* 2001; 15:297–309.
- [3] Collins DS, Pettitt WS, Young, RP. High-resolution mechanics of a microearthquake sequence. *Pure appl. Geophys.* 2002; 159:197–217.
- [4] Chang SH, Lee C-I. Estimation of cracking and damage mechanisms in rock under triaxial compression by moment tensor analysis of acoustic emission. *Int. J. Rock Mech. Min.* 2004; 41:1069–86.
- [5] Manthei G. Characterization of acoustic emission sources in a rock salt specimen under triaxial compression. *Bull. Seism. Soc. Am.* 2005; 95(5):1674–700.
- [6] Graham CC, Stanchits S, Main IG, Dresen G. Comparison of polarity and moment tensor inversion methods for source analysis of acoustic emission data. *Int. J. Rock Mech. Min.* 2010; 47:161–69.
- [7] Timms NE, Healy D, Reyes-Montes JM, Collins DS, Prior DJ, Young RP. Effects of crystallographic anisotropy on fracture development and acoustic emission in quartz. *J. Geophys. Res.* 2010; 115:B07202.
- [8] Kao CS, Carvalho FCS, Labuz JF. Micromechanisms of fracture from acoustic emission. *Int. J. Rock Mech. Min.* 2011, 48:666–73.
- [9] Vavryčuk V, Bohnhoff M, Jechumtálová Z, Kolář P, Šílený J. Non-double-couple mechanisms of micro-earthquakes induced during the 2000 injection experiment at the KTB site, Germany: A result of tensile faulting or anisotropy of a rock? *Tectonophysics.* 2008; 456:74–93.
- [10] Vavryčuk V. Inversion for anisotropy from non-double-couple components of moment tensors. *J. Geophys. Res.* 2004; 109:B07306.
- [11] Vavryčuk V. Tensile earthquakes: Theory, modeling, and inversion. *J. Geophys. Res.* 2011; 116: B12320.
- [12] Davi R, Vavryčuk V. Seismic network calibration for retrieving accurate moment tensors. *Bull. Seism. Soc. Am.* 2012; 102: 62491–06.
- [13] Frohlich C. Earthquakes with non-double-couple mechanisms. *Science.* 1994; 264:804–9.
- [14] Julian BR, Miller AD, Foulger GR. Non-double-couple earthquakes 1: Theory. *Rev. Geophys.* 1998; 36:525–49.
- [15] Miller AD, Foulger GR, Julian BR. Non-double-couple earthquakes 2: Observations. *Rev. Geophys.* 1998; 36:551–68.
- [16] Vavryčuk V. Inversion for parameters of tensile earthquakes. *J. Geophys. Res.* 2001; 106: B0816339–35.

- [17] Stanchits S, Fortin J, Gueguen Y, Dresen G. Initiation and propagation of compaction bands in dry and wet bentheim sandstone. *Pure Appl. Geophys.* 2009; 166:843-68. Doi: 10.1007/BF00876395.
- [18] Charalampidou EM, Hall SA, Stanchits S, Lewis H, Viggiani G. Characterization of shear and compaction bands in a porous sandstone deformed under triaxial compression. *Tectonophysics.* 2011; 503:8–17.
- [19] Stanchits S, Vinciguerra S, Dresen G. Ultrasonic velocities, acoustic emission characteristics and crack damage of basalt and granite. *Pure Appl. Geophys.* 2006; 163 (5-6):975-94. Doi:10.1007/s00024-006-0059-5.
- [20] Leonard M, Kennett BLN. Multi-component autoregressive techniques for analysis of the seismograms. *Phys. Earth Planet. Inter.* 1999; 113: (1-4) 247.
- [21] Nelder J, Mead R. A simplex method for function minimisation. *Comput. J.* 1965; 7:308-12.
- [22] Červený V. *Seismic Ray Theory.* Cambridge University Press, Cambridge; 2001.

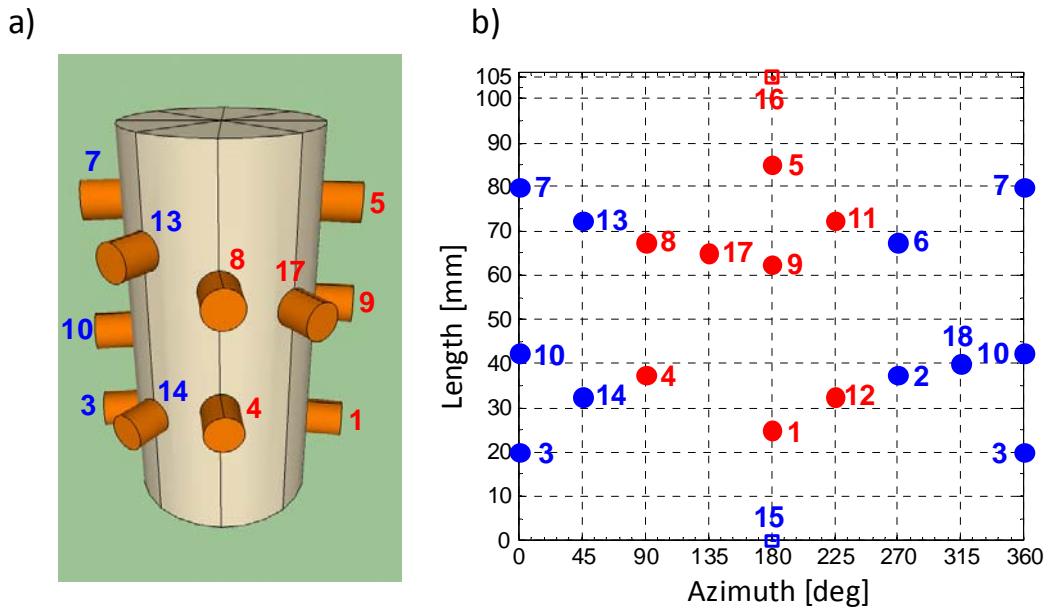


Figure 1. (a) Schematic plot of the positions of the AE sensors glued on the surface of the Bentheim specimen; (b) Azimuthal coverage of AE sensors used as receivers (in blue) and as receivers and transmitters (in red) as a function of the length of the specimen.

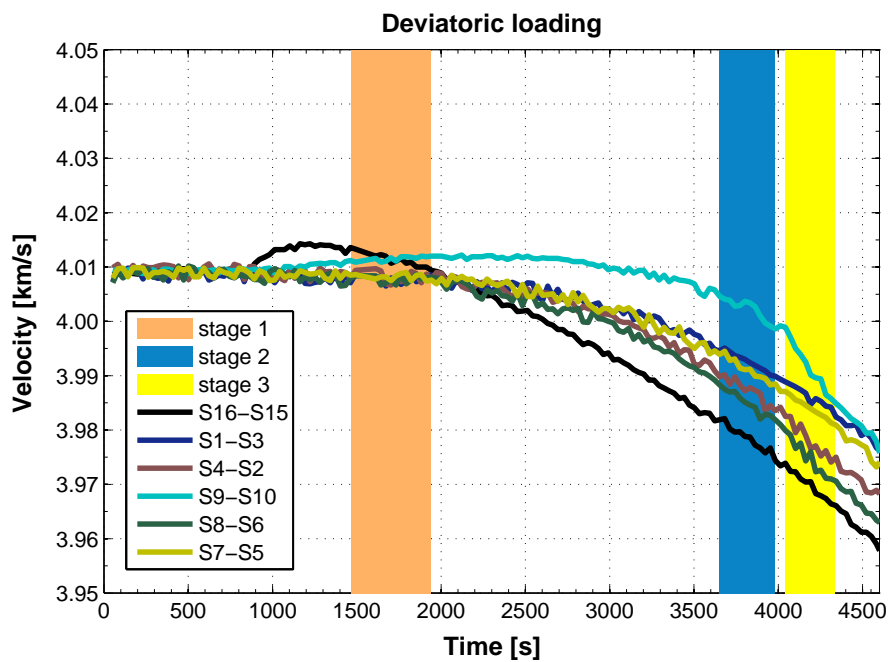


Figure 2. Velocity variations measured along rays between 6 transmitter-receiver pairs as a function of time. Three different time windows (stages) have been chosen for the network calibration and the moment tensor inversion.

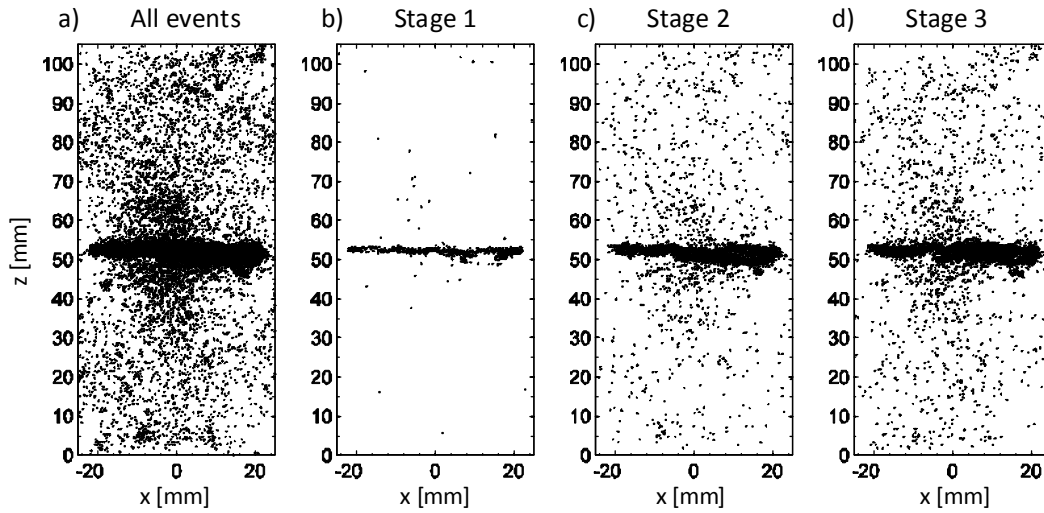


Figure 3. Hypocentre locations of acoustic emission events plotted in the x - z perpendicular projection: (a) the whole deviatoric stage; (b) time window: 1467-1940 s (stage 1); (c) time window: 3651-3980 s (stage 2); (d) time window: 4040-4335 s (stage 3).

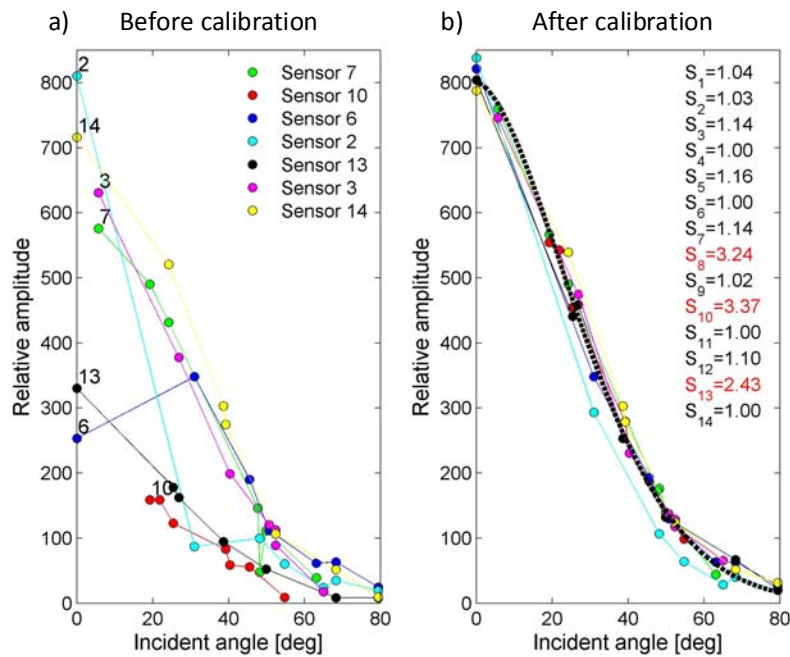


Figure 4. The amplitudes of recorded ultrasonic transmissions before (a) and after (b) calibration of AE sensors as a function of incidence angle for Bentheim sandstone. The raw and calibrated amplitude curves constructed from transmissions recorded at 7 receivers are shown in different colours corresponding to the ultrasonic receiver. The black numbers denotes the ultrasonic receiver. The assessed common calibration curve used in the correction of amplitudes for incidence angle and coupling is shown in plot (b) as the thick dashed line. The retrieved coupling factors (amplifications) due to applied calibration routine are show as table inset in plot (b).

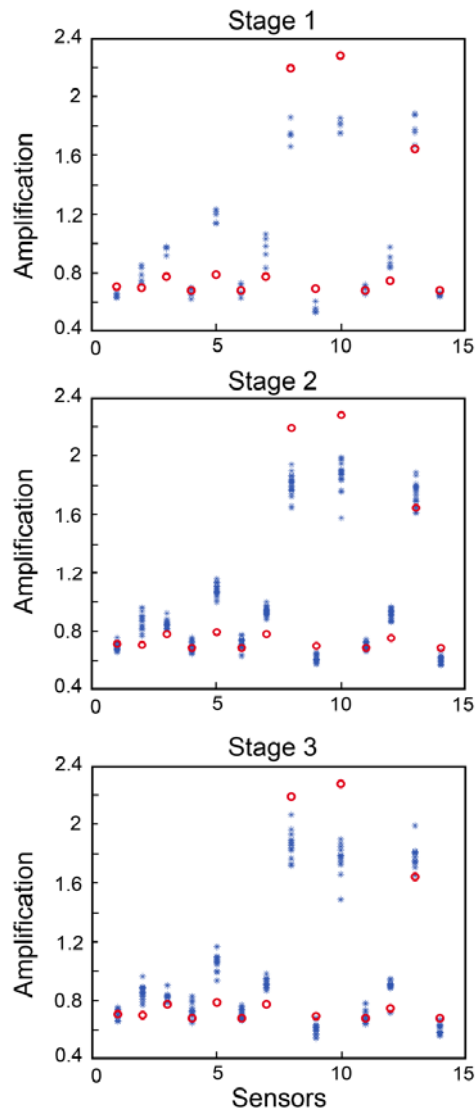


Figure 5. Sensor amplifications of uncalibrated (raw) data calculated for three selected stages. The amplifications are plotted for the individual 14 sensors. Each blue star represents a value calculated by the network calibration for one subset of 250 events. The clustering of amplifications indicates a high degree of stability with respect to event subsets. The red open circles show amplifications obtained by the ultrasonic calibration. The amplifications are normalized the average amplification of the complete set of sensors to be one.

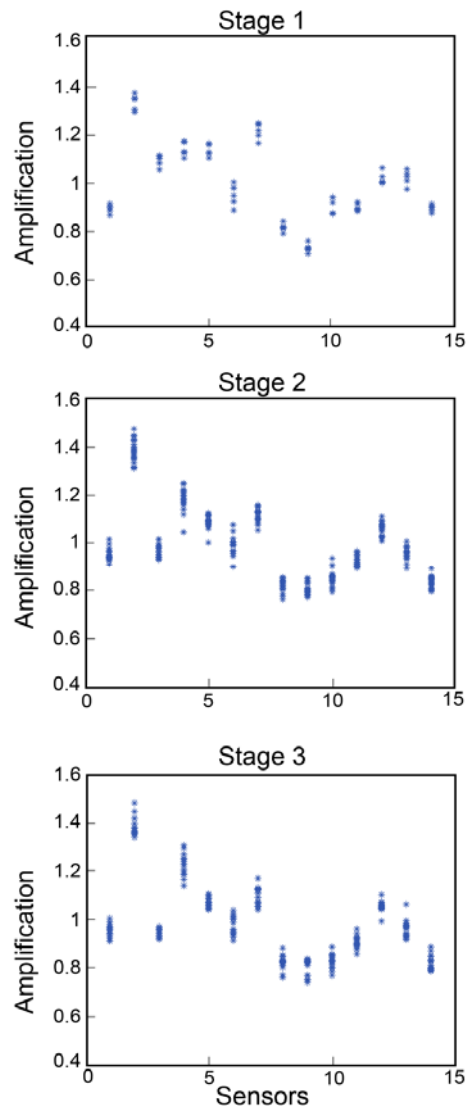


Figure 6. Sensor amplifications of ultrasonically calibrated data (see Section 4.1.) calculated for three selected stages. The amplifications are plotted for the individual 14 sensors. Each blue star represents a value calculated for one subset of 250 events. The clustering of amplifications indicates a high degree of stability with respect to event subsets.

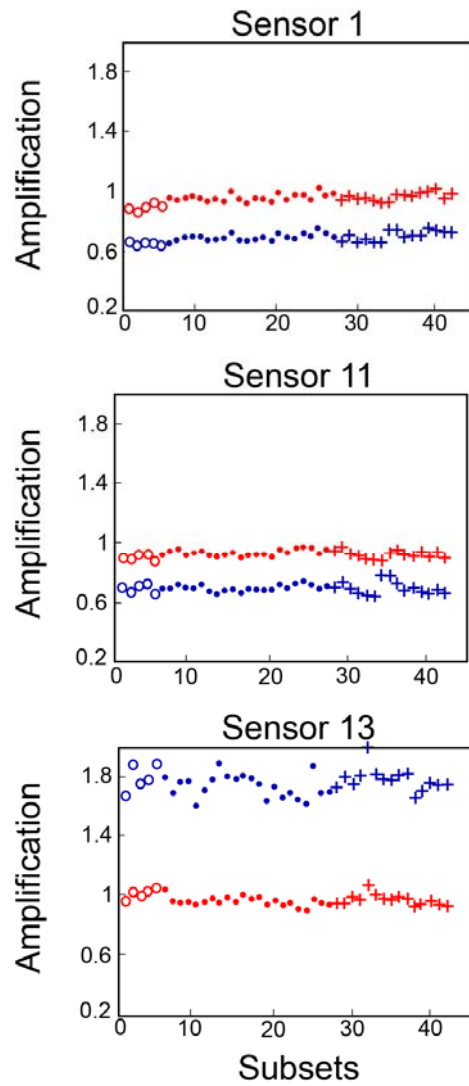


Figure 7. A comparison of the sensor amplifications calculated for ultrasonically calibrated (in red) and uncalibrated (in blue) data for three selected sensors (sensor 1, 11, 13) and for three stages (open circles for stage 1, dots for stage 2 and crosses for stage 3). Amplifications obtained from uncalibrated data show a higher level of scattering of amplification values with respect to calibrated data.

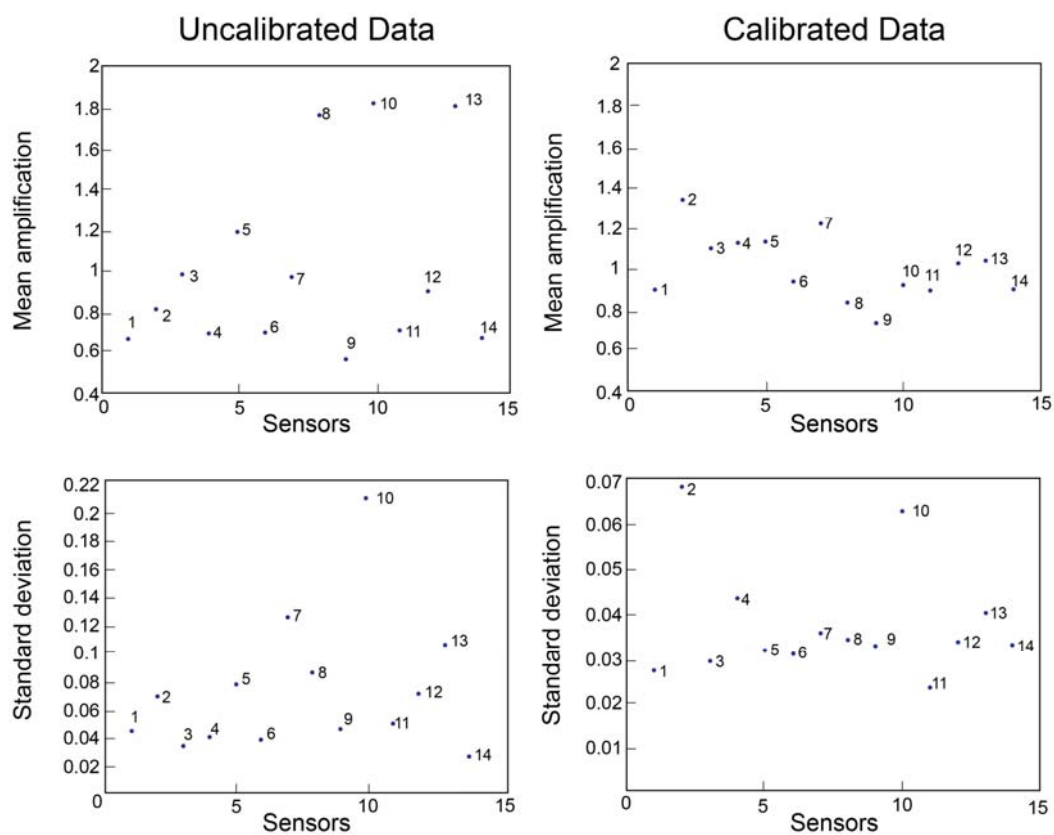


Figure 8. Mean values and standard deviations of sensor network amplifications calculated for uncalibrated (raw) and ultrasonically calibrated data. The mean values and the standard deviations are calculated from 50 values obtained by a repeating inversion of 100 randomly selected events. The numbers identify the sensors.

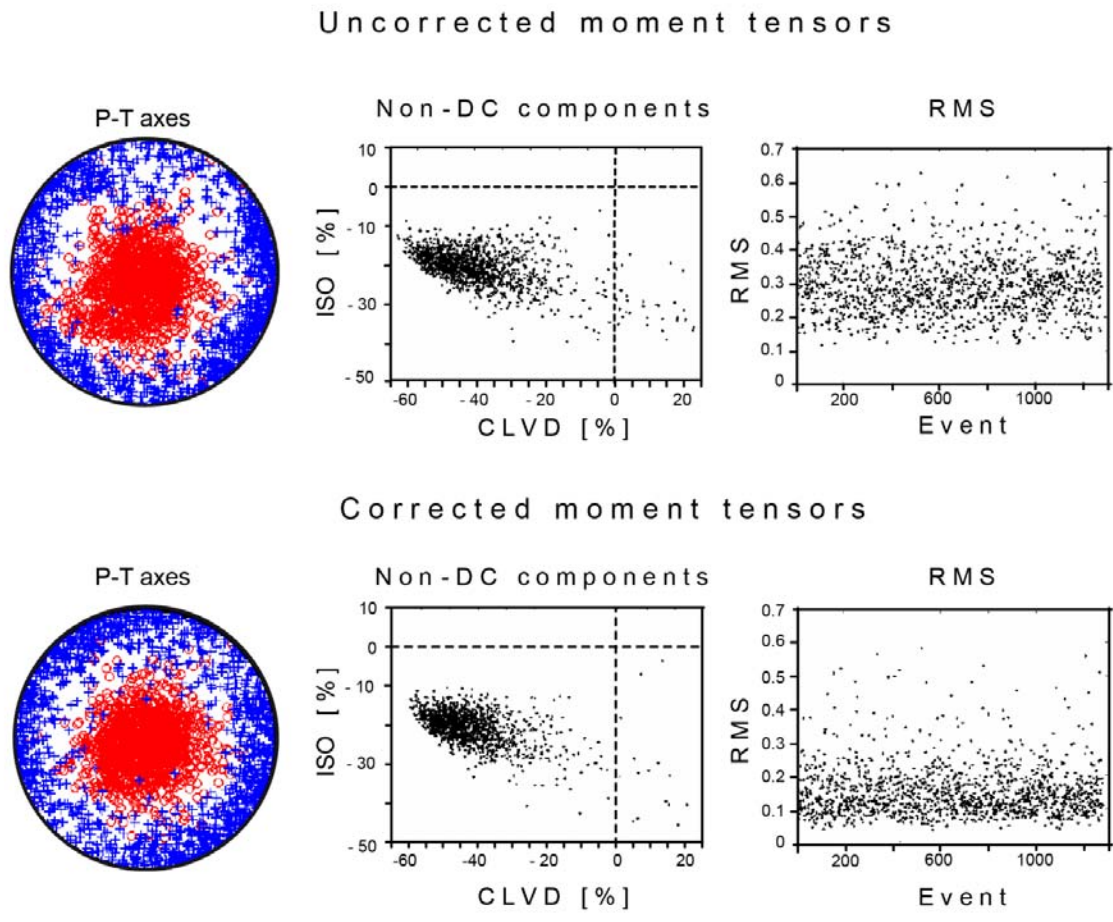


Figure 9. DC and non-DC components of the uncorrected and corrected moment tensors calculated from the uncalibrated (raw) data from stage 1. The corrected solutions show lower RMS values and more clustered non-DC components confirming the validity of the network calibration.

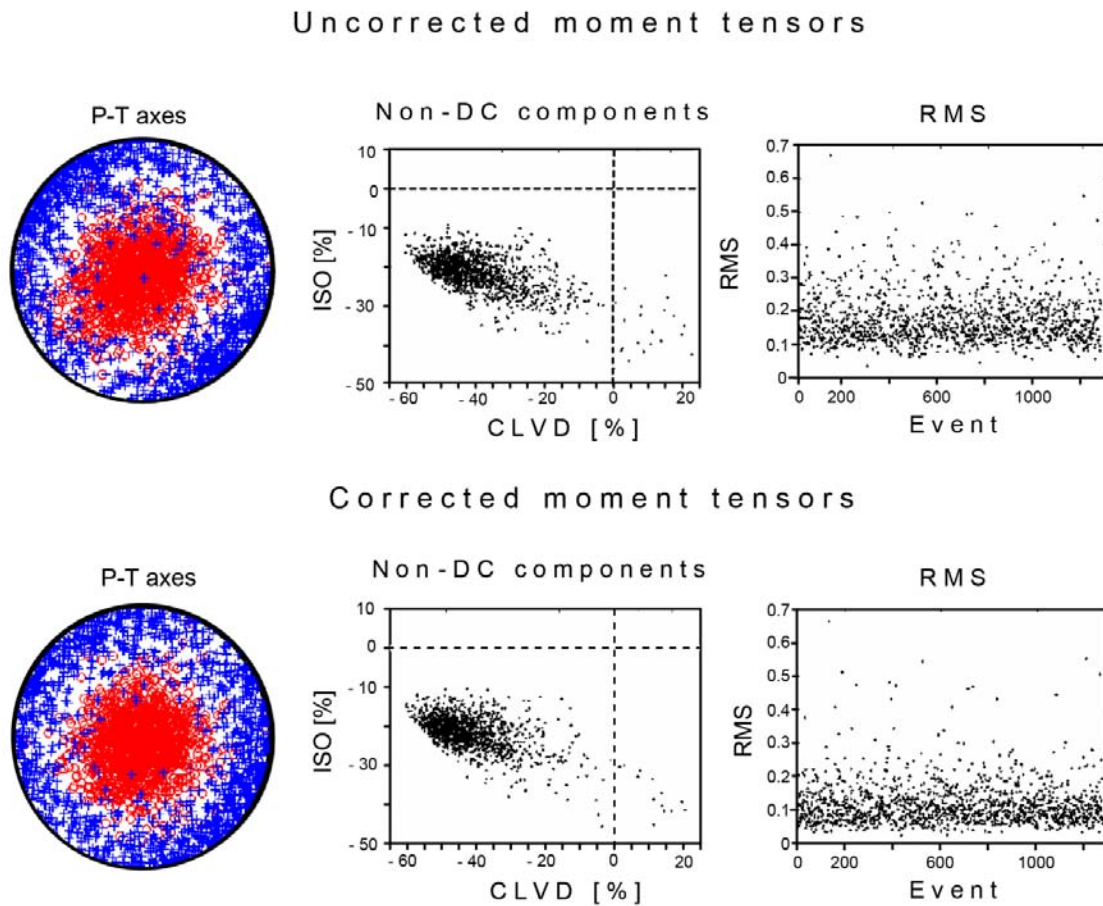


Figure 10. Same as for Figure 9 but for ultrasonically calibrated data.

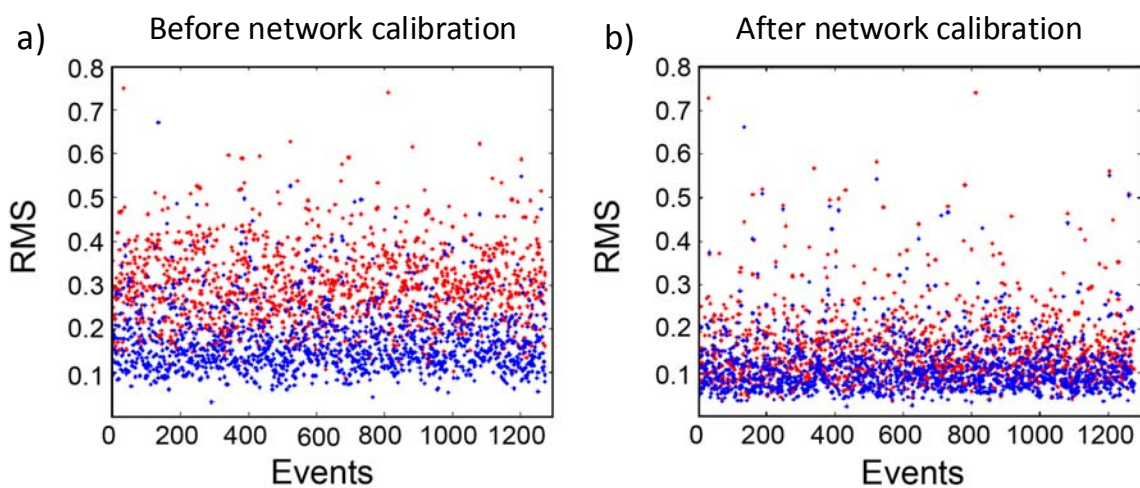


Figure 11. (a) A comparison of the RMS values obtained for uncorrected data and (b) for data corrected using the network calibration. Red – uncalibrated data, blue – ultrasonically calibrated data.